HHS Public Access

Author manuscript

J Mol Biol. Author manuscript; available in PMC 2020 July 12.

Published in final edited form as:

J Mol Biol. 2019 July 12; 431(15): 2700–2717. doi:10.1016/j.jmb.2019.05.019.

Solution Structure of the Carboxy-terminal Tandem Repeat Domain of Eukaryotic Elongation Factor 2 Kinase and its Role in Substrate Recognition

Andrea Piserchio[1], **Nathan Will**[1,2,¶], **David H. Giles**[3], **Fatlum Hajredini**[1,2], **Kevin N. Dalby**[3,4], and **Ranajeet Ghose**[1,2,5,6,*]

[1]Department of Chemistry and Biochemistry, The City College of New York, New York, NY 10031.

[2]Graduate Programs in Biochemistry, The Graduate Center of CUNY, New York, NY 10016.

[3]Graduate Program in Cell and Molecular Biology, University of Texas, Austin, TX 78712.

[4]Division of Chemical Biology and Medicinal Chemistry, University of Texas, Austin, TX 78712.

[5]Graduate Programs in Chemistry, The Graduate Center of CUNY, New York, NY 10016.

[6]Graduate Programs in Physics, The Graduate Center of CUNY, New York, NY 10016.

Abstract

Eukaryotic elongation factor 2 kinase (eEF-2K), an atypical calmodulin-activated protein kinase, regulates translational elongation by phosphorylating its substrate, eukaryotic elongation factor 2 (eEF-2), thereby reducing its affinity for the ribosome. The activation and activity of eEF-2K are critical for survival under energy-deprived conditions and is implicated in a variety of essential physiological processes. Previous biochemical experiments have indicated that the binding site for the substrate eEF-2 is located in the C-terminal domain of eEF-2K, a region predicted to harbor several α-helical repeats. Here, using NMR methodology we have determined the solution structure of a C-terminal fragment of eEF-2K, eEF-2K$_{562–725}$ that encodes two α-helical repeats. The structure of eEF-2K$_{562–725}$ shows signatures characteristic of TPR domains and of their SEL1-like sub-family. Further, using the analyses of NMR spectral perturbations and ITC measurements, we have localized the eEF-2 binding site on eEF-2K$_{562–725}$. We find that eEF-2K$_{562–725}$ engages eEF-2 with an affinity comparable to that of the full-length enzyme. Further, eEF-2K$_{562–725}$ is able to inhibit the phosphorylation of eEF-2 by full-length eEF-2K *in trans*. Our present studies establish that eEF-2K$_{562–725}$ encodes the major elements necessary to enable the eEF-2K/eEF-2 interactions.

*Correspondence: rghose@ccny.cuny.edu.

¶Current address: Laboratory of Molecular Electron Microscopy, The Rockefeller University, New York, NY 10065.

ACCESSION NUMBERS

The structure of eEF-2K$_{562–725}$ has been deposited into the PDB with ID 6NX4 and the corresponding chemical shifts have been deposited into the BMRB with accession code 30569.

INTRODUCTION

Eukaryotic elongation factor 2 kinase (eEF-2K), a key regulator of translational elongation, phosphorylates the GTPase, elongation factor 2 (eEF-2) on Thr-56[1]. This post-translational modification reduces the affinity of eEF-2 towards the ribosome[2–4], hinders the translocation of the nascent chain from the ribosomal A-site to the P-site, and leads to a reduction of global protein synthesis rates[5]. Given that protein synthesis constitutes one of the most energy consumptive processes in a eukaryotic cell[6], the activity of eEF-2K is critical for cytoprotection under a variety of energy-deprived conditions e.g. nutrient starvation[7], hypoxia[8] and genotoxic stress[9]. Since eEF-2K plays a central role in regulating a fundamental cellular process, its dysregulation has been linked to a variety of disease states, including several cancers[7;10;11], cardiovascular disease[12;13] and various neurological disorders, including Alzheimer's disease[14] and depression[15;16].

eEF-2K is activated by calmodulin (CaM) in a manner that diverges from other calmodulin-dependent kinases in that it does not entail a "release of inhibition" mechanism[17], but instead involves a two-step process initiated by the binding of calmodulin and subsequent autophosphorylation on a key Thr residue (T348)[18]. In addition to the primary activating phosphorylation on T348, eEF-2K is further regulated by a host of other phosphorylation events[19] that are mediated by several kinases, including PKA[20;21] and mTOR[14;22]. The activity of eEF-2K is also modulated by pH[23] and Ca^{2+} levels[24], making it a key integrator of diverse signal inputs, all working together to regulate translation.

A variety of mutational and deletion studies have helped define the organization of the functional "domains" (these are not necessarily structural domains, hence the quotes) of eEF-2K[25–27] shown schematically in Figure 1. These include a non-canonical calmodulin-binding domain (CBD) located at the N-terminus, followed by an α-kinase domain and a long regulatory loop (R-loop) that links to the C-terminal domain (CTD). The R-loop contains multiple phosphorylation sites including T348, whose phosphorylation is critical for fully activating the kinase, as mentioned above. The CTD is predicted to contain three helical repeats originally thought to be SEL1-like[28], and has been suggested to encode the binding-site for the substrate eEF-2[27]. However, an atomic resolution structure of full-length eEF-2K remains elusive, precluding further insight into its activation, activity and regulation in atomic detail. The significant sequence similarity of the eEF-2K catalytic domain with other members of the α-kinase sub-family, such as the ion-channel kinase, TRPM7 (28%)[29], and myosin heavy chain kinase A (MHCK A, 34%)[30] from *Dictyostelium discoideum*, makes homology modeling of this region feasible. Homology models of the catalytic domain have indeed been useful in a variety of biophysical[31] and biochemical studies[18;32]. However, this approach is somewhat difficult to extend to the rest of the protein, including the CTD, meaning that the overall protein architecture and the regulatory interactions among its various parts remains obscure. In parallel with our continuing efforts to obtain an atomic-resolution structure of intact eEF-2K, we have pursued a divide-and-conquer approach in obtaining high-resolution structures of its individual functional domains to assemble a model of the full-length enzyme using a hybrid approach[31]. To this end, we previously determined the solution structure of the eEF-2K CBD in complex with Ca^{2+}-calmodulin to define their primary interaction mode in atomic detail[33]. We had also solved the structure of the last C-

terminal helical repeat that comprises the CTD[34]. In these continuing efforts, we present here the high-resolution structure of a larger C-terminal fragment encompassing residues G562-E725 (eEF-2K$_{562–725}$). We had previously utilized the structure of eEF-2K$_{562–725}$, without any description or analysis of its features, in an integrative approach employing mass-spectrometric techniques and small angle X-ray scattering aided by computational methodology, to define the overall orientation of various domains of eEF-2K with respect to each other and Ca^{2+}-CaM in their complex[31]. We had stated in that manuscript that the structural features of the eEF-2K$_{562–725}$, that present a significant degree of uniqueness, would be presented elsewhere. Here, we describe the structure of eEF-2K$_{562–725}$ in detail. Further, utilizing this structure, and through the analyses of backbone amide and Ile, Leu, Met, Thr and Val methyl chemical shift perturbations, supported by amide cross-saturation measurements, we localize the site used by eEF-2K to engage its substrate, eEF-2. We show that eEF-2K$_{562–725}$ binds eEF-2 with an apparent affinity that is comparable to that of full-length eEF-2K. We further demonstrate that exogenous eEF-2K$_{562–725}$ efficiently inhibits the phosphorylation of eEF-2 by full-length eEF-2K *in vitro*. Taken together, these observations suggest that the most significant contributions to the recognition of eEF-2 by eEF-2K are encoded within the eEF-2K$_{562–725}$ fragment.

RESULTS AND DISCUSSION

Solution structure of eEF-2K$_{562–725}$

As described in detail in the Supplementary Materials, all constructs containing the first predicted[35] helical repeat of the eEF-2K CTD were found not to be amenable to detailed biophysical studies in isolation (Figures S1, S2). Therefore, eEF-2K$_{562–725}$, that encodes the final two predicted helical repeats of eEF-2K, was chosen for structure determination by NMR methods. As described in the Supplementary Materials, near complete assignment of backbone and sidechain resonances of eEF-2K$_{562–725}$ could be obtained (see Figure S3 for representative spectra). Before undertaking the laborious process of structure determination, in order to define the ordered regions of eEF-2K$_{562–725}$, we analyzed its steady-state $\{^1H\}-^{15}N$ NOE values (800 MHz; not shown). The region G562-G597 was found to be disordered with an average $\{^1H\}-^{15}N$ NOE value of 0.35 ± 0.08. Increased NOE values (0.78 ± 0.12) for the region encompassing residues F598-Q722 suggested that this segment was, on average, ordered and folded. The resulting NMR structural ensemble (Figure 2A; see Table 1 for experimental constraints and structure statistics) revealed the presence of six α-helical regions that were arranged in an approximatively anti-parallel fashion (Figure 2A), with angles between consecutive helices in the 129–164º range (see Table S2), resulting in an elongated structure. These helical regions (Figure 2B) encompass residues F598-A607 (B_{-3}), R610-D621 (A_{-2}), W634-M647 (B_{-2}), R664-T677 (A_{-1}), P686-A703 (B_{-1}) and G706-Q722, with the last sequence forming a C-terminal capping helix (Cp). The individual structures in the NMR ensemble form a tight cluster with backbone RMSD values (calculated for the helical regions with respect to an average conformation) of 0.43 (Figure 2A). Some of the loops that connect the individual helices retain this higher degree of order (Figure S4A), especially the short Cp-B_{-1} loop (M704-K705; average backbone RMSD 0.44 Å), the B_{-1}-A_{-1} loop (G678-D685; 0.87 Å), the A_{-2}-B_{-2} loop (S622-D633; 1.14 Å) and the short B_{-3}-A_{-2} loop (G608-D609; 0.62 Å). However, the long B_{-2}-A_{-1} loop (T648-P663)

exhibits the highest level of flexibility with an average backbone RMSD of 3.6 Å. As noted above, the extreme N-terminus remains largely unstructured with the exception of the region between P578 and I581, which consistently assumes turn-like configurations, and the region between E591 and T595, which populates either α-helical or turn-like conformations in the NMR ensemble (steady-state NOE values for both these regions are in the ~0.35 range).

Dynamic features of eEF-2K$_{562–725}$

To further validate the regions of order/disorder identified in the NMR-determined structural ensemble of eEF-2K$_{562–725}$, we performed a reduced spectral density analysis[36] using measured R_1, R_2 rates and steady-state $\{^1H\}-^{15}N$ NOE values. In line with the local RMSD values discussed above, J(0) values were found to be lowest (indicating the highest degree of flexibility) at the N-terminus, approximately up to residue N593 (1.5 ± 0.4 ns/rad; Figure S4B). In contrast, higher J(0) values (5.2 ± 0.8 ns/rad), indicative of a higher degree of rigidity (in the absence of exchange contributions), were seen for the helical regions. Interestingly, the magnitude of the J(0) values for the loop regions that include the longer 12-residue A_{-2}-B_{-2} loop were found to be only marginally smaller than those seen for the helical regions. The long 16-residue B_{-2}-A_{-1} loop showed significantly lower J(0) values (average 2.0 ± 0.7 ns/rad), with the lowest values being comparable to the unstructured N-terminal tail. These trends were mirrored by increased high frequency spectral density values ($J(0.87\omega_H)$; Figure S4C) at the N-terminus and the B_{-2}-A_{-1} loop, and reduced values in the helical regions and shorter loops. The plot of $J(\omega_N)$, the spectral density function at ^{15}N frequency, against J(0) (Figure S5) also indicates an overall clustering of values for the N-terminus, the extreme C-terminus and the B_{-2}–A_{-1} loop on the J(0)-$J(\omega_N)$ plane, suggesting that these regions share similar dynamic features. The corresponding values for the helical regions and the Cp-B_{-1}, B_{-1}-A_{-1}, A_{-2}-B_{-2} and B_{-3}-A_{-2} loops all cluster in close proximity to a Lorentzian curve expected for a rigid sphere, indicating that these regions approximate a single structural unit.

Comparison of the structures of eEF-2K$_{562–725}$ and eEF-2K$_{627–725}$

We had previously solved the structure of the final C-terminal helical repeat of eEF-2K in the context of a shorter eEF-2K$_{627–725}$ fragment[34]. The overall architecture of the eEF-2K$_{562–725}$ fragment is quite similar to that of eEF-2K$_{627–725}$ when comparing the A_{-1}, B_{-1} and Cp helices only (backbone RMSD = 0.85 Å, Figure S6). However, there are significant differences between the common regions of the two structures beyond this segment. In the structure of eEF-2K$_{627–725}$, the W634-A637 segment forms a disordered helix that does not make any specific contacts with the other helices. In the structure of eEF-2K$_{562–725}$, this segment is part of a stable B_{-2} helix (W634-M647) that packs against A_{-1} (and A_{-2}, a region that is absent in the eEF-2K$_{627–725}$ construct) to create the now well-defined second helical repeat. The stable packing of B_{-2} against the flanking helices generates a radically different conformation of the still long, though significantly shortened, B_{-2}-A_{-1} loop compared to the corresponding region in eEF-2K$_{627–725}$ (see Figure S6). The drastically altered structure in this region has significant consequences for the recognition of the substrate, eEF-2, as described below.

Similarities between eEF-2K$_{562–725}$ and other helical repeat domains

A search for structural homologs using the DALI server[37] reveals similarities between the folded helical region of eEF-2K$_{562–725}$ and several structures containing tetratricopeptide repeats (TPR; Table S3). For some, like Sec17 (Figure 3, PDB: 1QQE) that has the highest Z-score (11.3), the best matching segments are part of a much larger TPR domain; in other cases, like the human type II collagen prolyl 4-hydroxylase, the TPR-domain is of a size (Z-score 10.5, PDB: 6EVP, Figure 3) comparable to the ordered part of eEF-2K$_{562–725}$. A distinguishing feature of the overall structure of eEF-2K$_{562–725}$ is the fact that the loops that connect the helical regions are significantly longer than those seen in conventional TPR domains, in which loops that connect the intra-repeat (A_i-B_i) and the inter-repeat (B_i-A_{i+1}) helical regions are relatively short (~2 residues). The alternation of long intra-repeat loops, seen here for the A_{-1}-B_{-1} and A_{-2}-B_{-2} subunits, and of shorter inter-repeat loops, as observed for the B_{-1}-Cp and B_{-3}-A_{-2} subunits (Figure 2B), resemble a pattern that is characteristic of the structurally related SEL1-like repeat[28]. However, the B_{-2}-A_{-1} loop is anomalous, being far longer than the loop regions seen in other TPR or SEL-1 structures.

Alignment with an idealized TPR structure (PDB ID: 1NA0, DALI Z score = 9.0) reveals that most of the residues indicative of the TPR[38] signature occur at their expected positions in the structure of eEF-2K$_{562–725.}$ Cumulatively, the agreement with the aligned SMART consensus motifs for both TPR and SEL1-like[28] repeats is satisfied in approximately 80% of cases (Figure 4). There are, however, two key exceptions: E671 on helix A_{-1}, and G597 on helix B_{-3}. While S689 also deviates from Ala expected at this position, these two residue types share comparable steric profiles and helical propensities. The divergence of position 671 from the consensus (charged vs hydrophobic), was also noted in the structure of eEF-2K$_{627–725}$, and it was found to not adversely impact the packing of helix B_{-1} with the A_{-1} and Cp helices[34]. However, due to the disorder in the nascent B_{-2} helix in the structure of eEF-2K$_{627–725}$, this residue was found to be mostly solvent exposed. In contrast, for a significant subset of structures in the NMR ensemble of eEF-2K$_{562–725}$, this residue appears to engage in a favorable anion-π interaction[39] with residue Y641 from the now fully-formed and appropriately packed helix B_{-2}. The consensus residue at position 597 is an Ala, a small residue with a relatively high helical propensity. The Gly residue found at this position in the structure of eEF-2K$_{562–725}$ is also small but is a helix breaker. As expected, we observe that both K596 and G597 do not assume a helical configuration creating a rupture in helix B_{-3}. Surprisingly, this helix despite not having its partner in the eEF-2K$_{627–725}$ construct (the putative A_{-3}), docks stably against A_{-2}. However, compared to conventional TPR motifs, helix B_{-3} has a somewhat aberrant orientation that diverges significantly from that seen in the structural homologs of eEF-2K$_{562–725}$ (Figure 3). This is reflected in an A_{-2}-B_{-3} inter-helical angle (128.7 ± 3.0º) that is significantly smaller in magnitude than those seen in the other cases (Table S2). In order to test whether the anomalous orientation of helix B_{-3} is due to the absence of its partner, a predicted A_{-3} helix, we generated a longer construct, eEF-2K$_{541–725}$, that encompasses a region that is predicted to generate A_{-3}. Analysis of the chemical shifts using TALOS-N[40] suggested that the N-terminal extension did not alter the core structure of eEF-2K$_{562–725}$. This was also evident from the minimal perturbations in the backbone amide chemical shifts in the regions common to the two constructs (Figure S7A) and the chemical shift based order parameter values (RCI S^2)[41] (compare Figures S7B and

C). The only significant difference between the two constructs was the presence of a single helical turn centered around E565 (compare Figures S7D and E). Cumulatively the data indicated the absence of the predicted A_{-3} helix or an expansion of the tertiary fold beyond that found in eEF-2K$_{562–725}$.

Utilizing the structure of eEF-2K$_{562–725}$ described here, we had developed a model for a near-complete CTD, encompassing residues L496-E725[31] (Figure S8). In that model, the Q548–E576 region was composed of two antiparallel helices, both containing TPR-like sequence signatures. Given that an N-terminal extension of the eEF-2K$_{562–725}$ did not lead to an extension of the fold, we expect that the presence of a helix-breaking G597 instead of a consensus Ala and the resulting reduction in the helical surface may explain the inability of the preceding E541–S575 region in eEF-2K$_{541–725}$ to spontaneously form a A_{-3} helix and further extend the structural fold as expected. It is however possible that additional structured regions could form and be stabilized by long-range interactions in full-length eEF-2K, possibly with its α-kinase domain. It is notable, however, that our computational data do not suggest a TPR-like organization for the predicted helices preceding B_{-3}[31]. It is therefore possible that the TPR-like arrangement may be restricted to the region contained within the structure of eEF-2K562–725.

NMR analyses of the interaction between eEF-2K$_{562–725}$ and eEF-2

The C-terminal region of eEF-2K has been predicted to contain the binding site for the substrate eEF-2[27]. In our earlier studies we had found that eEF-2K$_{627–725}$ was unable to inhibit the phosphorylation of eEF-2 by eEF-2K under our experimental conditions, leading us to conclude that the binding site of eEF-2 was not wholly contained within this region of eEF-2K[34]. We tested if the longer eEF-2K$_{562–725}$ construct was able to bind eEF-2 using a combination of NMR methods. Several amide resonances were broadened out to beyond the threshold of detection, in addition to others that showed significant chemical shift perturbations (Figures 5A, S9), in a ^{15}N, ^{1}H TROSY spectrum of U-[^{15}N,^{2}H,^{13}C]-labeled eEF-2K$_{562–725}$ upon addition of an equimolar amount of yeast eEF-2. These spectral changes were widespread throughout the sequence, with the largest perturbations localized on the A_{-1}, B_{-1} and Cp helices. Some significant perturbations were also seen on the B_{-2} helix, on the B_{-2}-A_{-1} loop and on the B_{-1}-Cp loop (Figure 5A). Additional perturbations were also found on the flexible N-terminus, primarily in the Q576-L582 region. Perturbations for Ile (δ1), Leu (δ), Thr (γ2) and Val (γ) methyl groups were monitored using an ILVT-[^{15}N,^{2}H]-labeled eEF-2K$_{562–725}$ sample in the presence of a two-fold excess of eEF-2 and methyl ^{13}C, ^{1}H HMQC experiments (Figures 5B, S9). All of the expected methyl resonances were detectable, except for one of the two methyl groups of V568, which was not identifiable after eEF-2 binding. The largest methyl chemical shift changes were detected for I581 in the N-terminal region, and L708, located at the start of Cp. Significant shifts were also found for I567, the second methyl group of V568 (the other being broadened out in the presence of eEF-2), and L587, all located on the flexible N-terminal tail. Additional shifts were noted on I614 (A_{-2}), L626 (A_{-2}-B_{-2} loop), L645 (B_{-2}) and T694 (B_{-1}). The perturbations for the Met-ε positions were assessed using constant-time ^{13}C, ^{1}H HSQC experiments on U-[^{15}N,^{13}C]-labeled eEF-2K$_{562–725}$ in the presence of an equimolar amount of eEF-2. The largest shifts (Figure 5C) were seen for M701 (C-terminal part of B

$_{-1}$) and M704 (B_{-1}-Cp loop). A smaller, but significant, perturbation was also observed for M573 on the N-terminal region of the protein. Thus, in the presence of eEF-2, the largest perturbations of backbone amide and Ile, Leu, Met, Thr and Val methyl resonances were distributed over almost the entire Cp helix, the N-terminal region of the A_{-1} helix, the C-terminal regions of the B_{-1} and B_{-2} helices, and parts of the disordered regions of the protein including the N-terminus and the B_{-2}-A_{-1} loop.

In order to obtain additional confirmation of the surface utilized by eEF-2K$_{562–725}$ to engage eEF-2, we performed an amide-based cross-saturation experiment[42;43] on a sample of U-[^{15}N,^{2}H,^{13}C]-labeled eEF-2K$_{562–725}$ containing an equimolar amount of eEF-2. These experiments are typically performed in buffers containing a significant amount of D_2O in order to decrease the overall proton density and restrict spin diffusion to the molecular interface. However, the use of a large quantity of D_2O in the buffer would result in sensitivity losses in an already concentration-limited sample (80 μM in a 3 mm Shigemi tube). Therefore, we utilized a sample prepared in standard 95% H_2O-based buffer reasoning that, given the observed μM binding affinity (see below; compared with interactions in the nM range in the report by Shimada and coworkers[43]) and the resulting short lifetime of the bound state would limit the efficiency of the spin-diffusion within perdeuterated eEF-2K$_{562–725}$. Indeed, when discounting the largest outliers, the cross-saturation ratio (I_{sat}/I_{ref}) appeared to be rather homogeneous along the sequence (0.95±0.04; Figure S10), suggesting a limited spread of saturation effects beyond the immediate interaction site. The most significant attenuations (>2σ beyond the mean; σ=standard deviation) were observed at the start of helix A_{-1} (Y665), at the end of helix B_{-1} (A703) and on several residues located in the first half of Cp (A709, N710, Y713, K715). As pointed out earlier, the largest spectral perturbations were also localized in this region. However, despite the presence of obvious spectral perturbations (discussed above), no detectable attenuations were found in the N-terminal tail, or on the B_{-2}-A_{-1} loop. We attribute this to the fact that the large R_1 rates associated with these highly dynamic regions make saturation transfer less efficient compared to the more structured parts of eEF-2K$_{562–725}$. It is notable, however, that there is a systematic dip in I_{sat}/I_{ref} values for the B_{-2}-A_{-1} loop region, though these attenuations do not meet our highest >2σ threshold of significance (Figure S10).

eEF-2K$_{562–725}$ binds eEF-2 with micromolar affinity

Given that the NMR studies suggest that eEF-2K$_{562–725}$ interacts with eEF-2, we relied on isothermal titration calorimetry (ITC) measurements in order to characterize the binding affinity of the interaction. It has been reported that phosphorylation of eEF-2 on S595 by cyclin-A-cyclin-dependent kinase 2 enhances its interaction with eEF-2K[44]. However, we could not detect evidence of phosphorylation on S595 in our preparations of eEF-2 from yeast using LC-MS/MS. Given the modest heat release and resultant low overall sensitivity, ~2-fold variation in average K_D values was observed between measurements, with values ranging from 4.2 ± 1.4 to 8.9 ± 2.0 μM (see Table S4; also see Figure S11A for a representative isotherm). The K_D values determined here are comparable to K_M values previously obtained from steady-state kinetic measurements using tag-less recombinant eEF-2K and wheat-germ eEF-2 (K_M = 5.9 μM)[45]. A similar K_M value of 1.2 μM was also obtained when using GST-tagged eEF-2K and eEF-2 obtained from rabbit reticulocytes[25].

Thus, it is apparent that the most significant docking site(s) for eEF-2 are contained within the eEF-2K$_{562–725}$ construct.

Our NMR studies (described above) identified two spatially distinct regions of eEF-2K$_{562–725}$, namely the dynamic N-terminus and a C-terminal region encompassing the B_{-2}-A_{-1}-B_{-1}-Cp segment, that appear to play a role in binding eEF-2. The latter region appears to play a more significant role based on the distribution and magnitudes of the spectral perturbations. To test the relative contributions of these distinct regions to the binding free-energy, we generated a construct, eEF-2K$_{592–725}$ missing almost the entire the dynamic N-terminus, and measured its affinity for eEF-2 using ITC measurements (see Table S4; also see Figure S11B for a representative isotherm). The K_D values obtained for eEF-2K$_{592–725}$ were somewhat larger than those obtained for eEF-2K$_{562–725}$, and ranged from 15.4 ± 4.9 to 19.0 ± 4.6 μM, suggesting only a very modest contribution of the N-terminus of eEF-2K$_{562–725}$ towards its affinity for eEF-2.

A docking site for eEF-2 on eEF-2K

Combining the NMR and biophysical measurements it is apparent that the C-terminal region of eEF-2K, including parts of the A_{-1}, B_{-1}, B_{-2} and Cp helices, the B_{-1}-Cp loop, the dynamic B_{-2}-A_{-1} loop, make the most substantial contributions to the recognition of eEF-2. All of these elements localize in spatial proximity to each other, as shown in Figure 6. It is interesting that these regions are all present in primary sequence in eEF-2K$_{627–725}$, a construct that fails to inhibit the phosphorylation of eEF-2 by eEF-2K, producing a small (~14%) enhancement instead[34]. As described above, despite these regions being common to eEF-2K$_{562–725}$ and eEF-2K$_{627–725}$, several key elements show significant deviations between the two constructs. Most notably, the B_{-2} helix is only partially formed in eEF-2K$_{627–725}$ and does not pack against the A_{-1} helix. This also leads to a significantly longer B_{-2}-A_{-1} loop in the eEF-2K$_{627–725}$ construct that adopts a very different configuration compared to that in the eEF-2K$_{562–725}$ construct (Figure S6). Further, a fully formed B_{-2}-A_{-1}-B_{-1}-Cp assembly, that appears to be necessary to bind eEF-2, is only stable in the presence of the preceding A_{-2} helix. Thus, the dual domain tandem encompassing an intact A_{-2}-B_{-2}-A_{-1}-B_{-1}-Cp assembly, that exists in eEF-2K$_{562–725}$ (and in eEF-2K$_{592–725}$) but not in the eEF-2K$_{627–725}$, is required to create the appropriate docking elements for eEF-2.

Based on the biophysical studies described above we expected that, unlike eEF-2K$_{627–725}$, eEF-2K$_{562–725}$ would indeed be capable of inhibiting the phosphorylation of eEF-2 by full-length eEF-2K. We tested this possibility by measuring the ability of full-length eEF-2K to phosphorylate eEF-2 in the presence of varying amounts of eEF-2K$_{562–725}$ utilizing [γ $-^{32}$P]-labeled ATP and autoradiography. As shown in Figure 7, eEF-2K$_{562–725}$ inhibited eEF-2 phosphorylation with an IC_{50} or 18.5 ± 1.2 μM. Assuming one-site binding, this results in a K_i value of about 9 μM (assuming a 5.9 μM K_M) that is consistent with the K_D values obtained from the ITC measurements discussed above.

As shown in Figure 6, the eEF-2-induced perturbations on eEF-2K$_{562–725}$ appear to map onto a surface that is displaced toward the margins of its helical assembly, and seems to involve, in part, both its convex and concave faces. While employing both faces for binding

is not common for TPR domains, such a scenario has been observed before in the context of the PscE-PscF-PscG complex that regulates the formation of the type III secretion needle of *Pseudomonas aeruginosa*[46] (Figure S12). In this complex, the C-terminal helix from PscF binds the core of the concave face of the TPR domain-containing protein PscG, while PscE wraps around an edge of the TPR platform and engages both the concave and convex surfaces of PscG. We had previously developed a model for a near-full-length functional construct of eEF-2K[31]. In this model, a majority of the concave surface of the TPR region, including that contained within the eEF-2K$_{562–725}$ construct, was found to interact with the α-kinase domain of eEF-2K (Figure 8). Mapping the perturbations determined in the present study onto that structural model seems to suggest a mode of engagement of eEF-2 that is reminiscent of that seen in the PscE-PscF-PscG complex, wherein the CTD (including the eEF-2K$_{562–725}$ construct studied here) of eEF-2K plays the role of PscG, with the α-kinase domain of eEF-2K and eEF-2 playing the roles of PscF and PscE, respectively (compare Figures 8 and S12). However, the precise structural determinants of the eEF-2/eEF-2K interaction await the atomic-resolution structure of their complex.

Several mutation/deletion studies were previously carried out on eEF-2K, with some shown to abrogate eEF-2 phosphorylation[27]. As was noted in our previous work[34], the deleterious effects of these specific mutations/deletions on eEF-2 phosphorylation could be considered to be indirect, and the result of destabilization of the structural fold of the C-terminal region of eEF-2K. For example, deletion of fifteen C-terminal residues in eEF-2K[27] would destabilize the final helical repeat by removing the Cp helix in almost its entirety; a Y712A/Y713A mutation would eliminate several stabilizing interactions involving the Cp helix and unfold the repeat. These observations remain valid in the context of the structure of eEF-2K$_{562–725}$. However, it is also evident from work presented here that these alterations and the resultant structural destabilization would also disrupt the overall architecture of the eEF-2 recruitment site that is localized in this region, as suggested previously[27].

MATERIALS AND METHODS

Expression and purification of eEF-2K constructs

eEF-2K$_{562–725}$—The region encompassing residues G562-E725 of human eEF-2K was cloned into a pET-26b (Novagen) vector and transformed into either BL21 (DE3) cells (New England Biolabs), or BL21 (DE3) Star cells (Thermofisher). Typically, fresh colonies from an LB plate were picked to start a small-scale overnight bacterial growth at 37 °C, which was then used as a starter for 0.5 L of medium (LB or M9) in a 2 L baffled flask. At an OD$_{600}$ ~0.8, protein expression was induced with 0.4 M IPTG and incubated with shaking at 18 °C for 18 hours (24 hours when using a D_2O-based medium), then bacterial cells were spun down and stored at −80 °C. For U-[^{13}C,^{15}N]-labeled samples, 3 g/L of U-^{13}C D-glucose and 1 g/L of $^{15}NH_4Cl$ (99%) were used in the M9 medium. For the U-[^{13}C,^{15}N,^{2}H]-labeled samples, the cells were pre-equilibrated using a small volume bacterial culture in M9 medium containing increasing amounts of D_2O, as previously described[47]. After adaptation for growth in 100% D_2O, the cells were used to start a 250 mL (using a 1 L flask) culture in a D_2O-based M9 medium containing 3 g/L of U-[^{13}C,^{2}H] D-glucose and 1 g/L $^{15}NH_4Cl$. A similar strategy was adopted for the production of the ILVT-U-[^{15}N,^{2}H]-labeled sample. The

medium was prepared using U-^{2}H-labeled D-glucose and 1 g/L $^{15}NH_4Cl$; 50 mg/L of (methyl-^{13}C; 3,3-^{2}H2) sodium α-ketoisobutyrate and 100 mg/L of (3-methyl-^{13}C; 3,4,4,4-^{2}H4) sodium α-ketoisovalerate were added to the growth 1 hour before induction; 50 mg/L of (4-^{13}C; 2–3 $^{2}H_2$) L-threonine, together with 100 mg/L of ^{2}H-labeled glycine were added at the time of induction. The cells were resuspended in buffer containing 50 mM Tris pH 7.8, 0.5 M NaCl, 150 mM KCl, 0.1% TritonX, lysed by sonication and centrifuged at 17000 g for 20 minutes. The supernatant was then loaded onto a metal affinity column (Cobalt Agarose Beads, High Density, Gold Biotechnology), washed with lysis buffer containing 3 mM imidazole, and eluted with 0.4 M imidazole. The solution was then dialyzed against 20 mM Tris pH 7.8, 100 mM KCl, 2.5 mM $CaCl_2$, 0.1% β-mercaptoethanol; thrombin (Enzyme Research Laboratories, 2 units/mg) was present in the dialysis bag. The following day the completeness of the N-terminal His-tag cleavage was confirmed by SDS-PAGE analysis. Then the solution was loaded onto a HiTrap Q HP column (GE Healthcare), washed with buffer containing 20 mM Tris pH 8.0, 200 μM EDTA, 2 mM DTT (buffer A) and eluted with a 4.7 mM NaCl/mL gradient. eEFK-2K$_{562–725}$ (containing an N-terminal SHM cloning artifact) that eluted as a single peak at ~0.42 M NaCl (~33.23 mS/cm) was concentrated using spin-column and injected into a gel filtration column (Superdex-75, GE Healthcare) pre-equilibrated with NMR buffer (20 mM phosphate pH 6.5, 100 mM NaCl, 4 mM DTT, 200 μM EDTA) as a final purification step.

eEF-2K$_{592–725}$—A construct encompassing residues E592-E725 of human eEF-2K was sub-cloned by PCR from the eEF-2K$_{562–725}$ vector (see above), and re-inserted into a pET-26b vector by DNA ligation using the same NdeI and BamHI restriction sites. Protein expression and purification of the natural abundance sample was done in LB medium using the methodology listed above for eEF-2K$_{562–725}$ for use in the ITC measurements.

eEF-2K$_{541–725}$—A pET-28b vector (Thermofisher) encoding an N-terminal $(His)_6$-tag, followed by a SUMO-tag and residues E541-E725 of human eEF-2K was obtained starting from the analogous eEF-2K$_{490–725}$ construct (see Supplementary Material), where the middle 490–540 segment was deleted using the Q5 cloning kit (New England Biolabs). The vector was then transformed into BL21 (DE3) Star cells (Thermofisher), and the natural abundance and U-[^{15}N,^{13}C]-labeled samples were expressed as described above for eEF-2K$_{562–725}$. The expressed protein was dialyzed against a buffer containing 20 mM Tris pH 7.5, 200 mM NaCl, 0.1% β–mercaptoethanol, 200 μM EDTA, in the presence of Ulp1. Spin columns were employed to exchange into buffer A (see above) and to lower the solution conductivity, after which the protein of interest was isolated from the cleavage mixture using anion exchange (elution around 0.4 M NaCl, 37.7 mS/cm) and further purified using size exclusion chromatography, as described above for eEF-2K$_{562–725}$.

eEF-2—eEF-2 was purified from commercial yeast cake (obtained from The New York Bakers, interestingly based in San Diego, CA) using previously published protocols[48]. Briefly, about 100 g of the yeast cake was suspended in ~200–300 mL of ice-cold buffer containing 20 mM HEPES pH 7.2, 10% glycerol, 300 mM KCl, 5 mM $MgCl_2$, 1 mM DTT and 1 mM PMSF, loaded on a bead beater using a 1/1 (v/v) sample/beads (0.5 mm) ratio. The blender was activated for 16 minutes total, with a 1 minute on and 1 minute off schedule

and using an ice slush/NaCl mixture for refrigeration. The sample was centrifuged first for 20 minutes at 15000 g, and then ultra-centrifuged at 45000 rpm (158,000 g at r_{av}) on a 45 TI rotor (Beckman Coulter) for 1 hour. The pH was adjusted to 7.2 by direct Tris (1 M) titration, and dialyzed against 20 mM HEPES pH 7.2, 10% glycerol, 5 mM $MgCl_2$, 1 mM DTT, until the conductivity was below 4 mS/cm. After further centrifugation and filtering, the sample was loaded onto a HiPrep SP FF 16/10 (GE Healthcare), and eluted using a 6.5% per CV gradient of 150 mM KCl. 10% SDS-PAGE gels assessed the location of eEF-2 (typically between 5.6 and 8.4 mS/cm). After manual adjustment of the pH and filtration, the protein was loaded onto a HiTrap Q HP column (GE Healthcare) pre-equilibrated with 20 mM Tris pH 7.8, 5 mM $MgCl_2$, 1 mM DTT, 10% glycerol, and eluted using a 1% per CV gradient (typically between 10 and 30%) of 1 M KCl. The elution peak (~20.4 mS/cm) was then concentrated and loaded onto a Superdex200 equilibrated with either NMR (see above) or ITC buffer (see below). The identity of the protein was confirmed by western blot analysis (rabbit anti-eEF-2 primary antibody #2332S, Cell Signaling Technology) and mass spectrometry.

NMR Spectroscopy

All NMR experiments were acquired at 25 °C on Bruker spectrometers operating at 600–900 MHz, all equipped with cryogenic probes capable of applying pulsed-field gradients along the z-axis. All NMR samples were dissolved in the NMR buffer (see above) in the presence of 2 mM AEBSF and 5% ^2H_2O (for locking). For the measurement of residual dipolar couplings, the following buffer was used - 14 mM phosphate pH 6.5, 100 mM NaCl, 4 mM DTT, 200 μM EDTA, and ~14 mg/mL Pf1 phage (Asla Biotech). For samples containing eEF-2, NaCl in the NMR buffer was replaced by KCl and samples also contained 5% (v/v) of $^2H_6$-glycerol (the $^2H_6$-glycerol vs glycerol exchange was done using spin columns) for methyl-based experiments. A protease inhibitor cocktail (protease Inhibitor mini tablets, EDTA-free, Pierce) was added to the buffer to prevent sample degradation. All experiments were processed with NMRPipe[49] and analyzed using NMRView[50]. Non-uniformly sampled (NUS) data were generated using the Poisson Gap Sampling method[51] and processed using the IST algorithm[52], except for the 4-dimensional ^{13}C-HSQC-NOESY-^{15}N-HSQC experiment, which was processed using SMILE[53].

Resonance assignment and generation of structural constraints

The concentrations of the U-[^{13}C,^{15}N]-labeled eEF2K$_{562–725}$ samples for the resonance assignment procedure ranged between 200 to 600 μM, and 4 mm or 5 mm Shigemi tubes were used in the experiments. Backbone assignments were obtained using the standard set of gradient-enhanced triple resonance experiments collected at various fields including HNCO, HN(CA)CO, HNCACB, HN(CA)CB, CBCA(CO)NH, HNCA, HN(CO)CA. Resonances corresponding to the aliphatic sidechains of eEF2K$_{562–725}$ were assigned using H(CCCO)NH, (H)C(CCO)NH, HC(C)H, and (H)CCH experiments (see Table S1). Resonances for the aromatic sidechains of eEF-2K$_{562–725}$ were obtained using a 3-dimensional ^{13}C-NOESY-HSQC optimized for aromatic resonances; the sidechain amino positions of Asn and Gln residues and the Arg Hε/Nε resonances were assigned using a 3-dimensional ^{15}N-NOESY-HSQC, and the Met-ε resonances were assigned using a 4-dimensional ^{13}C-HSQC-NOESY-^{13}C-HSQC experiment. Distance restraints were derived

from the 3-dimensional ^{15}N-NOESY-HSQC and 3-dimensional ^{13}C-NOESY-HSQC experiments mentioned above, a 3-dimensional ^{13}C-NOESY-HSQC (optimized for aliphatic resonances), a 3-dimensional ^{15}N,^{15}N-HSQC-NOESY-HSQC, and a 4-dimensional ^{13}C-HSQC-NOESY-^{15}N-HSQC. All of the NOESY experiments used mixing times of 150 milliseconds. Amide ^{15}N,^{1}H residual dipolar coupling (RDC) values were obtained from 2D HSQC-IPAP[54] experiments (700 MHz) on a 400 μM sample of eEF-2K$_{562–725}$ in the presence and absence of 14 mg/mL of Pf1 phage. NC' RDCs were also obtained at 700 MHz on a similar sample using an IPAP-J-HNCO experiment[55] and an accordion value of 3.

Structure calculations

Peak intensities derived from the NOE experiments mentioned above and backbone dihedral angle restraints derived from TALOS-N[40] were introduced into a ARIA2.3 structure calculation protocol[56;57] using standard options. The RDC values (HN and NC') for regions of defined secondary structure were introduced using the SANI option starting from the 5th ARIA iteration. The required rhombicity and tensor magnitude values were derived independently for each set using PALES[58] from a previous structure calculation run that did not use RDC restraints. Violation tolerance was automatically adjusted and force field softening[59] was introduced, otherwise the protocol was identical to what previously employed for the structure calculations of eEF-2K$_{627–725}$[34]. On each iteration, 1000 structures were generated, of which 100 retained for analysis. The final NMR ensemble comprised of 100 structures, of which the 20 lowest energy structures were analyzed using PROCHECK-NMR[60], the WHATIF web-server[61] and the PSVS web-server[62] and deposited in the PDB with accession code 6NX4 (see Table 1 for constraints, statistics of the final NMR ensemble of 100 structures, and structural characteristics of 20 lowest energy structures deposited into the PDB).

Amide ^{15}N relaxation measurements

A steady state {^{1}H}–^{15}N NOE experiment[63] was acquired using a 7.0 second recycling delay without (reference) or with a 5.0 second ^{1}H saturation period using 512 and 120 complex points in the direct and indirect dimension (13.0 and 33.0 ppm spectral windows), respectively. R_1 rates were measured using the following relaxation delays: 5.0, 20.0, 50.0 (x2), 100.0, 200.0, 400.0, 800.0, 1200.0 and 1600.0 milliseconds, with 512 (13 ppm) and 120 (33 ppm) complex points in the direct and indirect dimensions, respectively. R_2 rates were measured using the following relaxation delays: 0.0, 14.1 (x2), 28.2, 42.3, 56.4, 70.5 (x2) and 127.0 milliseconds, with 512 (13 ppm) and 128 (33 ppm) complex points in the direct and indirect dimensions, respectively. All relaxation measurements were performed at 800 MHz.

The resonance intensities for each relaxation delay were obtained using NMRView[50], and the corresponding rates were calculated using non-linear least squares fits to single-exponential decay curves. Errors were estimated using jack-knife resampling. Errors in the {^{1}H}–^{15}N steady-state NOEs were calculated using:

$$\sigma_{NOE} = \frac{I_{sat}}{I_{ref}}\sqrt{\left(\frac{\sigma_{sat}}{I_{sat}}\right)^2 + \left(\frac{\sigma_{ref}}{I_{ref}}\right)^2} \quad (1)$$

Where $I_{sat/ref}$ and $\sigma_{sat/ref}$ represent the intensities and the noise, respectively for the saturated/reference experiments. A similar formula was employed to calculate errors on the cross-saturation transfer ratios described below. Reduced spectral density functions were calculated from the relaxation data using a script within the software RELAX[64;65].

NMR-based titrations

All NMR-based titrations were performed at 800 MHz using 3 mm Shigemi tubes. Backbone amide chemical shift perturbations induced by eEF-2 were derived from a ^{15}N, ^{1}H TROSY experiment (1024 and 225 complex points, 13.4 and 31.2 ppm spectral windows in the direct and indirect dimension, respectively) collected on an 80 μM sample of U-[^{15}N,^{2}H, ^{13}C]-labeled eEF-2K$_{562–725}$ containing an equimolar amount of unlabeled eEF-2. Methyl chemical shift perturbations for Ile (δ_1), Leu (δ), Val (γ), and Thr (γ_2) positions were obtained from a methyl ^{13}C, ^{1}H SOFAST-HMQC[66] experiment that utilized a 0.2 seconds recycle delay. 512 and 192 complex points with 13.9 and 18.5 ppm spectral windows were used in the direct and indirect dimensions, respectively. Data were collected on a 40 μM ILVT-U-[^{15}N,^{2}H]-labeled eEF-2K$_{562–725}$ sample containing with 80 μM unlabeled eEF-2. ^{13}C, ^{1}H SOFAST-HMQC experiments were also collected at intermediate concentrations of eEF-2 to track resonances and aid in the resonance assignment of the bound state. In all cases, reference spectra were collected under similar buffer conditions. Met-ε perturbations were obtained from a constant-time (13.3 milliseconds) ^{13}C,^{1}H HSQC using a 50 μM sample of U-[^{15}N,^{2}H,^{13}C]-labeled eEF-2K$_{562–725}$ containing unlabeled eEF-2 in an equimolar ratio. The experiment utilized 1024 and 256 complex points with 16.0 and 72.0 ppm spectral windows in the direct and indirect dimensions, respectively. Chemical shift perturbation values ($\Delta\delta$) were calculated using the following equation[67]

$$\Delta\delta_j = \sqrt{0.5\sum_i \left(\frac{\delta_{ij}}{\sigma_i^k}\right)^2} \quad (2)$$

Where j is the residue number, i is the nucleus type (^{1}H, ^{15}N or ^{13}C), and σ_i^k is the standard deviation obtained from the Biological Magnetic Resonance Databank (BMRB) for nucleus type i and amino acid type k.

Cross-saturation measurements

An amide ^{1}H saturation transfer[42] experiment was collected on an 80 μM U-[^{15}N,^{2}H,^{13}C]-labeled sample of eEF-2K$_{562–725}$ containing an equimolar amount of eEF-2 by the application of a 2.0 second train of 10.5 millisecond Gaussian ^{1}H π pulses, each sandwiched between two 9.0 millisecond delays and centered at 0.82 ppm, immediately followed by a ^{15}N, ^{1}H TROSY experiment (1024 and 192 complex points, 13.4 and 31.2 ppm spectral

windows in the direct and indirect dimensions, respectively). For the reference spectrum, the carrier for saturation was moved to −20.00 ppm. The reference and saturated experiments were collected in an interleaved manner to minimize errors. Cross-saturation data were plotted as intensity ratios, and the experimental errors were calculated using Equation (1) as in the case of the steady-state $\{^1H\}-^{15}N$ NOE experiments (see above).

Isothermal titration calorimetry (ITC) measurements

Both the titrant and the analyte were co-dialyzed against the ITC buffer (20 mM MES pH 6.5, 200 mM EDTA, 5% glycerol, 100 mM KCl, 1 mM TCEP) and brought to desired concentrations using spin columns. Samples were degassed extensively before use in the ITC measurements. For titrations using eEF-2K$_{562–725}$ (in the syringe) and eEF-2 (in the cell), the concentrations were the following: 363.1 μM in the syringe and 27.6 μM in the cell (two titrations), 585.9 μM in the syringe and 35.2 μM in the cell (two titrations). Isotherms (19 usable data-points) were collected on an iTC200 (Malvern) at 25 ºC, with a 600 rpm stirring speed, a reference power of 10 μCal/sec, 2 μL injection volumes over 4.0 seconds, with a 180 second delay between injections. For each titration, a reference isotherm was collected by injecting the same titrant solution into a cell filled with buffer only. After subtraction, the curves were analyzed using the one-site binding model using the Origin software provided by the vendor. For titrations using eEF-2K$_{592–725}$ (in the syringe) and eEF-2 (in the cell), the concentrations were the following: 29 μM in the cell and 585.9 μM in the syringe (two titrations) (see Table S4).

Competition Assays

eEF-2K$_{562–725}$ was first exchanged five times into kinase buffer containing 25 mM HEPES pH 7.5, 50 mM KCl, 10 mM $MgCl_2$, 150 μM $CaCl_2$, 0.1 mM EGTA, and 5 Mm DTT using a 5 kDa cutoff centrifugal concentrator. Phosphorylation of eEF-2 (6 μM) at varying concentrations of eEF-2K$_{562–725}$ (1.55, 3.10, 6.20, 12.40, 24.81, 49.63, 99.25 and 198.5 μM) was measured in kinase buffer containing 2 μM CaM and 10 μg/mL BSA. Reactions were initiated by addition of [$\gamma-^{32}$P]-ATP and full-length eEF-2K to final concentrations of 1.0 mM and 0.2 nM, respectively, at 30 °C. After five minutes, a 10 μL aliquot of this reaction (5.6 μg of eEF-2) was removed and placed into SDS-PAGE loading buffer containing a final concentration of 50 mM EDTA. Reaction aliquots were boiled and loaded onto a 10% polyacrylamide gel for electrophoresis and separation of phosphorylated eEF-2. Gels were Coomassie stained and destained according to established protocols to visualize total eEF-2, and used to expose X-ray film to quantify relative levels of eEF-2 phosphorylation (autoradiography). Bands corresponding to eEF-2 were excised and placed in scintillation fluid in order to determine the incorporation of radioactive phosphate. Counts per minute (CPM) were plotted as a function of eEF-2K$_{562–725}$ concentration, [eEF2K$_{562–725}$], in GraphPad Prism and fit to the following equation to estimate the concentration giving 50% maximal inhibition (IC_{50})

$$CPM_{\log\left[eEF2K_{562-725}\right]} = CPM_{\min} + \frac{CPM_{\max} - CPM_{\min}}{1 + 10^{\log\left[eEF2K_{562-725}\right] - \log IC_{50}}} \quad (3)$$

Where $CPM_{\log\left[eEF2K_{562-725}\right]}$ is the measured CPM at a given concentration of eEF-2K$_{562–725}$; CPM$_{max}$ and CPM$_{min}$ are the maximum and minimum measurements, respectively. All measurements were performed in duplicate.

Supplementary Material

Refer to Web version on PubMed Central for supplementary material.

ACKNOWLEDGEMENTS

This work is supported by NIH R01 GM123252 (to RG and KND) and Welch F-1390 (KND). RG is a member of the New York Structural Biology Center, a NYSTAR facility. NW and FH acknowledge support from the United States Department of Education GAANN awards P200A120211 and P200A150068, respectively.

REFERENCES

1. Nairn AC, Bhagat B & Palfrey HC (1985). Identification of calmodulin-dependent protein kinase III and its major M_r 100,000 substrate in mammalian tissues. Proc. Natl. Acad. Sci. USA 82, 7939–43. [PubMed: 3906654]
2. Carlberg U, Nilsson A & Nygard O (1990). Functional properties of phosphorylated elongation factor 2. Eur. J. Biochem 191, 639–45. [PubMed: 2390990]
3. Ryazanov AG & Davydova EK (1989). Mechanism of elongation factor 2 (EF-2) inactivation upon phosphorylation. Phosphorylated EF-2 is unable to catalyze translocation. FEBS Lett 251, 187–90. [PubMed: 2753158]
4. Dumont-Miscopein A, Lavergne JP, Guillot D, Sontag B & Reboud JP (1994). Interaction of phosphorylated elongation factor EF-2 with nucleotides and ribosomes. FEBS Lett 356, 283–6. [PubMed: 7805855]
5. Ryazanov AG, Shestakova EA & Natapov PG (1988). Phosphorylation of elongation factor 2 by EF-2 kinase affects rate of translation. Nature 334, 170–3. [PubMed: 3386756]
6. Buttgereit F & Brand MD (1995). A hierarchy of ATP-consuming processes in mammalian cells. Biochem J 312, 163–7. [PubMed: 7492307]
7. Leprivier G, Remke M, Rotblat B, Dubuc A, Mateo AR, Kool M, Agnihotri S, El-Naggar A, Yu B, Prakash Somasekharan S, Faubert B, Bridon G, Tognon CE, Mathers J, Thomas R, Li A, Barokas A, Kwok B, Bowden M, Smith S, Wu X, Korshunov A, Hielscher T, Northcott PA, Galpin JD, Ahern CA, Wang Y, McCabe MG, Collins VP, Jones RG, Pollak M, Delattre O, Gleave ME, Jan E, Pfister SM, Proud CG, Derry WB, Taylor MD & Sorensen PH (2013). The eEF2 kinase confers resistance to nutrient deprivation by blocking translation elongation. Cell 153, 1064–79. [PubMed: 23706743]
8. Connolly E, Braunstein S, Formenti S & Schneider RJ (2006). Hypoxia inhibits protein synthesis through a 4E-BP1 and elongation factor 2 kinase pathway controlled by mTOR and uncoupled in breast cancer cells. Mol. Cell. Biol 26, 3955–3965. [PubMed: 16648488]
9. Kruiswijk F, Yuniati L, Magliozzi R, Low TY, Lim R, Bolder R, Mohammed S, Proud CG, Heck AJ, Pagano M & Guardavaccaro D (2012). Coupled activation and degradation of eEF2K regulates protein synthesis in response to genotoxic stress. Science Signal 5, ra40.
10. Liu R & Proud CG (2016). Eukaryotic elongation factor 2 kinase as a drug target in cancer, and in cardiovascular and neurodegenerative diseases. Acta Pharmacol. Sin 37, 285–94. [PubMed: 26806303]
11. Meric-Bernstam F, Chen H, Akcakanat A, Do KA, Lluch A, Hennessy BT, Hortobagyi GN, Mills GB & Gonzalez-Angulo AM (2012). Aberrations in translational regulation are associated with poor prognosis in hormone receptor-positive breast cancer. Breast Cancer Res 14, R138. [PubMed: 23102376]

12. Usui T, Okada M, Hara Y & Yamawaki H (2013). Eukaryotic elongation factor 2 kinase regulates the development of hypertension through oxidative stress-dependent vascular inflammation. Am. J. Physiol. Heart Circ. Physiol 305, H756–68. [PubMed: 23812389]
13. Chan AY, Soltys CL, Young ME, Proud CG & Dyck JR (2004). Activation of AMP-activated protein kinase inhibits protein synthesis associated with hypertrophy in the cardiac myocyte. J. Biol. Chem 279, 32771–9. [PubMed: 15159410]
14. Li X, Alafuzoff I, Soininen H, Winblad B & Pei JJ (2005). Levels of mTOR and its downstream targets 4E-BP1, eEF2, and eEF2 kinase in relationships with tau in Alzheimer's disease brain. FEBS J 272, 4211–20. [PubMed: 16098202]
15. Kavalali ET & Monteggia LM (2012). Synaptic Mechanisms Underlying Rapid Antidepressant Action of Ketamine. Am. J. Psychiatry 169, 1150–1156. [PubMed: 23534055]
16. Monteggia LM, Gideons E & Kavalali ET (2013). The role of eukaryotic elongation factor 2 kinase in rapid antidepressant action of ketamine. Biol. Psych 73, 1199–203.
17. Crivici A & Ikura M (1995). Molecular and structural basis of target recognition by calmodulin. Annu. Rev. Biophys. Biomol. Struct 24, 85–116. [PubMed: 7663132]
18. Tavares CD, Ferguson SB, Giles DH, Wang Q, Wellmann RM, O'Brien JP, Warthaka M, Brodbelt JS, Ren P & Dalby KN (2014). The molecular mechanism of eukaryotic elongation factor 2 kinase activation. J. Biol. Chem 289, 23901–16. [PubMed: 25012662]
19. Redpath NT, Price NT, Severinov KV & Proud CG (1993). Regulation of elongation factor-2 by multisite phosphorylation. Eur. J. Biochem 213, 689–99. [PubMed: 8386634]
20. Diggle TA, Redpath NT, Heesom KJ & Denton RM (1998). Regulation of protein-synthesis elongation-factor-2 kinase by cAMP in adipocytes. Biochem. J 336, 525–9. [PubMed: 9841860]
21. Diggle TA, Subkhankulova T, Lilley KS, Shikotra N, Willis AE & Redpath NT (2001). Phosphorylation of elongation factor-2 kinase on serine 499 by cAMP-dependent protein kinase induces Ca^{2+}/calmodulin-independent activity. Biochem. J 353, 621–6. [PubMed: 11171059]
22. Browne GJ & Proud CG (2004). A Novel mTOR-regulated phosphorylation site in elongation factor 2 kinase modulates the activity of the kinase and its binding to calmodulin. Mol. Cell. Biol 24, 2986–2997. [PubMed: 15024086]
23. Xie J, Mikolajek H, Pigott CR, Hooper KJ, Mellows T, Moore CE, Mohammed H, Werner JM, Thomas GJ & Proud CG (2015). Molecular mechanism for the control of eukaryotic elongation factor 2 kinase by pH: role in cancer cell survival. Mol. Cell. Biol 35, 1805–24. [PubMed: 25776553]
24. Tavares CD, Giles DH, Stancu G, Chitjian CA, Ferguson SB, Wellmann RM, Kaoud TS, Ghose R & Dalby KN (2017). Signal Integration at elongation factor 2 kinase; the roles of calcium, calmodulin and Ser-500 phosphorylation. J. Biol. Chem 292, 2032–2045. [PubMed: 27956550]
25. Pavur KS, Petrov AN & Ryazanov AG (2000). Mapping the functional domains of elongation factor-2 kinase. Biochemistry 39, 12216–24. [PubMed: 11015200]
26. Diggle TA, Seehra CK, Hase S & Redpath NT (1999). Analysis of the domain structure of elongation factor-2 kinase by mutagenesis. FEBS Lett 457, 189–92. [PubMed: 10471776]
27. Pigott CR, Mikolajek H, Moore CE, Finn SJ, Phippen CW, Werner JM & Proud CG (2012). Insights into the regulation of eukaryotic elongation factor 2 kinase and the interplay between its domains. Biochem. J 442, 105–18. [PubMed: 22115317]
28. Mittl PR & Schneider-Brachert W (2007). Sel1-like repeat proteins in signal transduction. Cell. Signal 19, 20–31. [PubMed: 16870393]
29. Yamaguchi H, Matsushita M, Nairn AC & Kuriyan J (2001). Crystal structure of the atypical protein kinase domain of a TRP channel with phosphotransferase activity. Mol. Cell 7, 1047–57. [PubMed: 11389851]
30. Ye Q, Crawley SW, Yang Y, Cote GP & Jia Z (2010). Crystal structure of the alpha-kinase domain of Dictyostelium myosin heavy chain kinase A. Science Signal 3, ra17.
31. Will N, Lee K, Hajredini F, Giles DH, Abzalimov RR, Clarkson M, Dalby KN & Ghose R (2018). Structural dynamics of the activation of elongation factor 2 kinase by Ca^{2+}-calmodulin. J. Mol. Biol 430, 2802–2821. [PubMed: 29800565]

32. Devkota AK, Edupuganti R, Yan C, Shi Y, Jose J, Wang Q, Kaoud TS, Cho EJ, Ren P & Dalby KN (2014). Reversible covalent inhibition of eEF-2K by carbonitriles. ChemBioChem 15, 2435–2442. [PubMed: 25224652]
33. Lee K, Alphonse S, Piserchio A, Tavares CD, Giles DH, Wellmann RM, Dalby KN & Ghose R (2016). Structural basis for the recognition of eukaryotic elongation factor 2 kinase by calmodulin. Structure 24, 1441–51. [PubMed: 27499441]
34. Will N, Piserchio A, Snyder I, Ferguson SB, Giles DH, Dalby KN & Ghose R (2016). Structure of the C-terminal helical repeat domain of eukaryotic elongation factor 2 kinase. Biochemistry 55, 5377–86. [PubMed: 27571275]
35. Prakash A, Jeffryes M, Bateman A & Finn RD (2017). The HMMER web server for protein sequence similarity search. Curr. Protoc. Bioinform 60, 3.15.1–3.15.23.
36. Farrow NA, Zhang O, Forman-Kay JD & Kay LE (1995). Comparison of the backbone dynamics of a folded and an unfolded SH3 domain existing in equilibrium in aqueous buffer. Biochemistry 34, 868–78. [PubMed: 7827045]
37. Holm L & Rosenstrom P (2010). Dali server: conservation mapping in 3D. Nucleic Acids Res 38, W545–9. [PubMed: 20457744]
38. Main ERG, Xiong Y, Cocco MJ, D'Andrea L & Regan L (2003). design of stable α-helical arrays from an idealized TPR motif. Structure 11, 497–508. [PubMed: 12737816]
39. Wang DX & Wang MX (2013). Anion-pi interactions: generality, binding strength, and structure. J. Am. Chem. Soc 135, 892–7. [PubMed: 23244296]
40. Shen Y & Bax A (2013). Protein backbone and sidechain torsion angles predicted from NMR chemical shifts using artificial neural networks. J. Biomol. NMR 56, 227–41. [PubMed: 23728592]
41. Berjanskii MV & Wishart DS (2005). A simple method to predict protein flexibility using secondary chemical shifts. J. Am. Chem. Soc 127, 14970–1. [PubMed: 16248604]
42. Nakanishi T, Miyazawa M, Sakakura M, Terasawa H, Takahashi H & Shimada I (2002). Determination of the interface of a large protein complex by transferred cross-saturation measurements. J. Mol. Biol 318, 245–9. [PubMed: 12051834]
43. Takahashi H, Nakanishi T, Kami K, Arata Y & Shimada I (2000). A novel NMR method for determining the interfaces of large protein-protein complexes. Nature Struct. Biol 7, 220–3. [PubMed: 10700281]
44. Hizli AA, Chi Y, Swanger J, Carter JH, Liao Y, Welcker M, Ryazanov AG & Clurman BE (2013). Phosphorylation of eukaryotic elongation factor 2 (eEF2) by cyclin A-cyclin-dependent kinase 2 regulates its inhibition by eEF2 kinase. Mol. Cell. Biol 33, 596–604. [PubMed: 23184662]
45. Abramczyk O, Tavares CD, Devkota AK, Ryazanov AG, Turk BE, Riggs AF, Ozpolat B & Dalby KN (2011). Purification and characterization of tagless recombinant human elongation factor 2 kinase (eEF-2K) expressed in Escherichia coli. Prot. Expr. Purif 79, 237–44.
46. Quinaud M, Ple S, Job V, Contreras-Martel C, Simorre JP, Attree I & Dessen A (2007). Structure of the heterotrimeric complex that regulates type III secretion needle formation. Proc. Natl. Acad. Sci. USA 104, 7803–8. [PubMed: 17470796]
47. Piserchio A, Nair PA, Shuman S & Ghose R (2010). Solution NMR studies of Chlorella virus DNA ligase-adenylate. J. Mol. Biol 395, 291–308. [PubMed: 19913033]
48. Kaul G, Pattan G & Rafeequi T (2011). Eukaryotic elongation factor-2 (eEF2): its regulation and peptide chain elongation. Cell. Biochem. Funct 29, 227–34. [PubMed: 21394738]
49. Delaglio F, Grzesiek S, Vuister GW, Zhu G, Pfeifer J & Bax A (1995). NMRPipe: a multidimensional spectral processing system based on UNIX pipes. J. Biomol. NMR 6, 277–93. [PubMed: 8520220]
50. Johnson BA (2018). From raw data to protein backbone chemical shifts using NMRFx processing and NMRViewJ analysis. Meth. Mol. Biol 1688, 257–310.
51. Hyberts SG, Takeuchi K & Wagner G (2010). Poisson-gap sampling and forward maximum entropy reconstruction for enhancing the resolution and sensitivity of protein NMR data. J. Am. Chem. Soc 132, 2145–7. [PubMed: 20121194]

52. Hyberts SG, Milbradt AG, Wagner AB, Arthanari H & Wagner G (2012). Application of iterative soft thresholding for fast reconstruction of NMR data non-uniformly sampled with multidimensional Poisson Gap scheduling. J. Biomol. NMR 52, 315–27. [PubMed: 22331404]
53. Ying J, Delaglio F, Torchia DA & Bax A (2017). Sparse multidimensional iterative lineshape-enhanced (SMILE) reconstruction of both non-uniformly sampled and conventional NMR data. J. Biomol. NMR 68, 101–118. [PubMed: 27866371]
54. Yao L, Ying J & Bax A (2009). - Improved accuracy of ^{15}N-^{1}H scalar and residual dipolar couplings from gradient-enhanced IPAP-HSQC experiments on protonated proteins. J. Biomol. NMR 43, 161–70. [PubMed: 19205898]
55. Permi P, Rosevear PR & Annila A (2000). - A set of HNCO-based experiments for measurement of residual dipolar couplings in ^{15}N, ^{13}C, ^{2}H-labeled proteins. J. Biomol. NMR 17, 43–54. [PubMed: 10909865]
56. Bardiaux B, Malliavin T & Nilges M (2012). ARIA for solution and solid-state NMR. Meth. Mol. Biol 831, 453–83.
57. Habeck M, Rieping W, Linge JP & Nilges M (2004). NOE assignment with ARIA 2.0: the nuts and bolts. Meth. Mol. Biol 278, 379–402.
58. Zweckstetter M (2008). NMR: prediction of molecular alignment from structure using the PALES software. Nature Protoc 3, 679–690. [PubMed: 18388951]
59. Mareuil F, Malliavin TE, Nilges M & Bardiaux B (2015). Improved reliability, accuracy and quality in automated NMR structure calculation with ARIA. J. Biomol. NMR 62, 425–38. [PubMed: 25861734]
60. Laskowski RA, Rullmannn JA, MacArthur MW, Kaptein R & Thornton JM (1996). AQUA and PROCHECK-NMR: programs for checking the quality of protein structures solved by NMR. J. Biomol. NMR 8, 477–86. [PubMed: 9008363]
61. Vriend G (1990). WHAT IF: a molecular modeling and drug design program. J. Mol. Graph 8, 52–6, 29. [PubMed: 2268628]
62. Bhattacharya A, Tejero R & Montelione GT (2007). Evaluating protein structures determined by structural genomics consortia. Proteins 66, 778–95. [PubMed: 17186527]
63. Ferrage F, Cowburn D & Ghose R (2009). Accurate sampling of high-frequency motions in proteins by steady-state ^{15}N-{^{1}H} nuclear Overhauser effect measurements in the presence of cross-correlated relaxation. J. Am. Chem. Soc 131, 6048–6049. [PubMed: 19358609]
64. d'Auvergne EJ & Gooley PR (2008). Optimisation of NMR dynamic models II. A new methodology for the dual optimisation of the model-free parameters and the Brownian rotational diffusion tensor. J. Biomol. NMR 40, 121–33. [PubMed: 18085411]
65. d'Auvergne EJ & Gooley PR (2008). Optimisation of NMR dynamic models I. Minimisation algorithms and their performance within the model-free and Brownian rotational diffusion spaces. J. Biomol. NMR 40, 107–19. [PubMed: 18085410]
66. Amero C, Schanda P, Dura MA, Ayala I, Marion D, Franzetti B, Brutscher B & Boisbouvier J (2009). Fast two-dimensional NMR spectroscopy of high molecular weight protein assemblies. J. Am. Chem. Soc 131, 3448–9. [PubMed: 19243101]
67. Piserchio A, Ramakrishan V, Wang H, Kaoud TS, Arshava B, Dutta K, Dalby KN & Ghose R (2015). Structural and dynamic features of F-recruitment site driven substrate phosphorylation by ERK2. Sci. Rep 5, 11127. [PubMed: 26054059]
68. Kenney JW, Moore CE, Wang X & Proud CG (2014). Eukaryotic elongation factor 2 kinase, an unusual enzyme with multiple roles. Adv. Biol. Regul 55, 15–27. [PubMed: 24853390]
69. Perraud AL, Zhao X, Ryazanov AG & Schmitz C (2011). The channel-kinase TRPM7 regulates phosphorylation of the translational factor eEF2 via eEF2-k. Cell. Signal 23, 586–93. [PubMed: 21112387]
70. Wang X, Regufe da Mota S, Liu R, Moore CE, Xie J, Lanucara F, Agarwala U, Pyr Dit Ruys S, Vertommen D, Rider MH, Eyers CE & Proud CG (2014). Eukaryotic elongation factor 2 kinase activity is controlled by multiple inputs from oncogenic signaling. Mol. Cell. Biol 34, 4088–103. [PubMed: 25182533]
71. Tavares CD, O'Brien JP, Abramczyk O, Devkota AK, Shores KS, Ferguson SB, Kaoud TS, Warthaka M, Marshall KD, Keller KM, Zhang Y, Brodbelt JS, Ozpolat B & Dalby KN (2012).

Calcium/calmodulin stimulates the autophosphorylation of elongation factor 2 kinase on Thr-348 and Ser-500 to regulate its activity and calcium dependence. Biochemistry 51, 2232–45. [PubMed: 22329831]

- eEF-2K regulates translational elongation by phosphorylating eEF-2 resulting in the latter's reduced affinity for the ribosome.
- The C-terminal region of eEF-2K has been predicted to contain the binding site for eEF-2.
- We have determined the structure of a C-terminal fragment (eEF-2K$_{562–725}$) of eEF-2K that encodes its last two helical repeats.
- Using biochemical and biophysical analysis we demonstrate that eEF-2K$_{562–725}$ contains the key elements necessary for the eEF-2K/eEF-2 interaction.

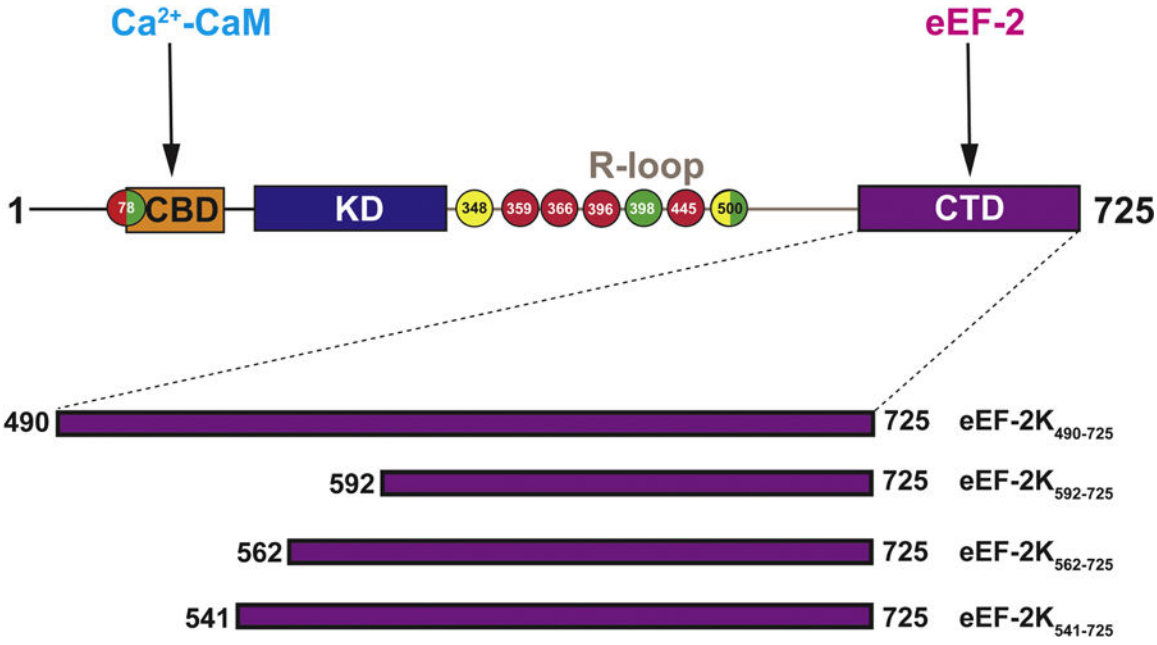

Figure 1.

Schematic representation of the functional domains of eEF-2K. The N-terminal calmodulin-binding domain (orange; targeted by Ca^{2+}-calmodulin), the α-kinase domain (dark blue) and the C-terminal domain (CTD; purple), predicted to encode the binding site for the substrate, eEF-2 are depicted. The kinase domain and CTD are connected by the regulatory loop (R-loop) which contains multiple phosphorylation sites (depicted as spheres)[68]. The site (T348) of primary activating auto-phosphorylation, upregulating and downregulating phosphorylation are shown in yellow, green and red, respectively. The N-terminal phosphorylation site S78 has been proposed to play both a positive[69] and a negative[70] regulatory role through unique mechanisms. S500 is also a key site for regulatory auto-phosphorylation[24;71], in addition to being targeted by PKA[21]. Also shown schematically are CTD constructs that are referred to in the manuscript.

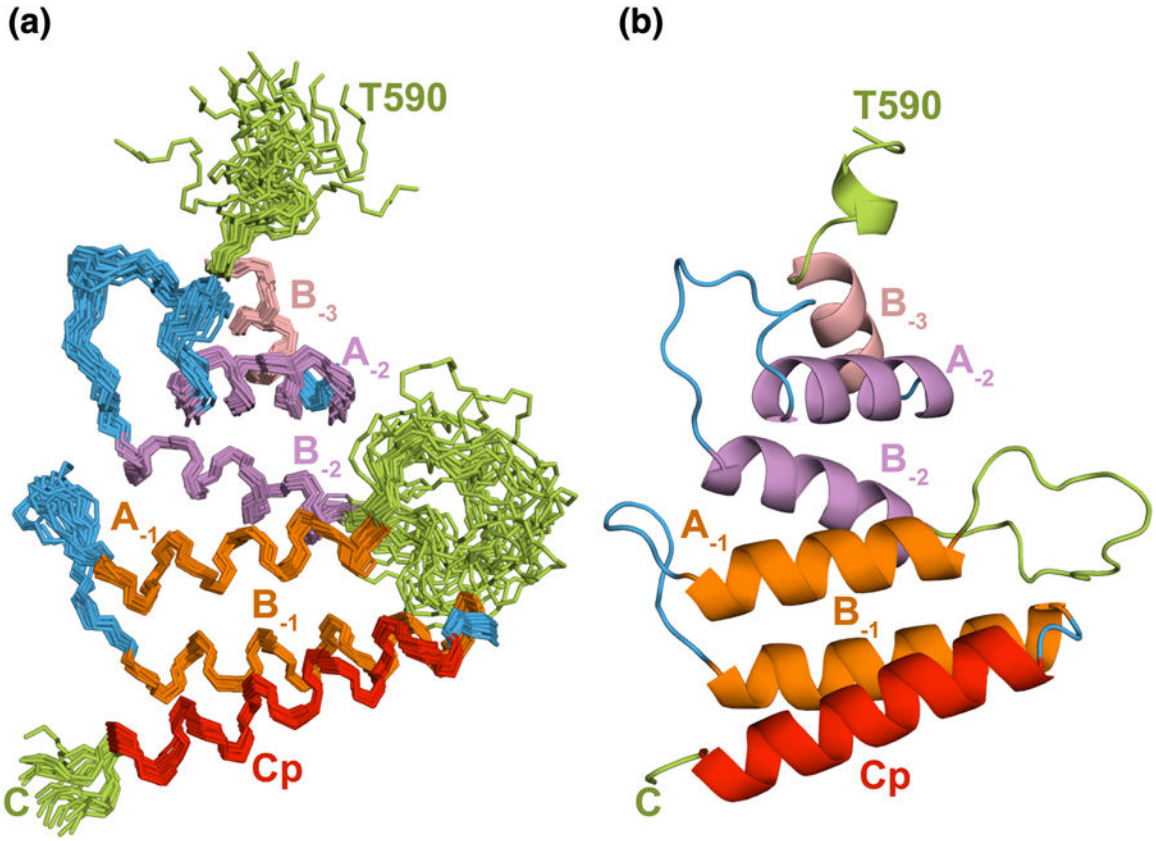

Figure 2.

(A) Backbone traces of 20 lowest energy conformers in the NMR-determined structural ensemble of $eEF2K_{562–725}$. Only a portion of the unstructured N-terminus is shown for clarity. The helical regions are colored as follows - pink (B_{-3}), violet (A_{-2}, B_{-2}), orange (A_{-1}, B_{-1}), and red (Cp; capping helix). The loops that show a relatively higher degree of order are colored blue. The highly disordered regions, including the $A_{-2}B_{-1}$ loop are colored light green. **(B)** Ribbon representation of a representative structure from the solution ensemble of $eEF2K_{562–725}$.

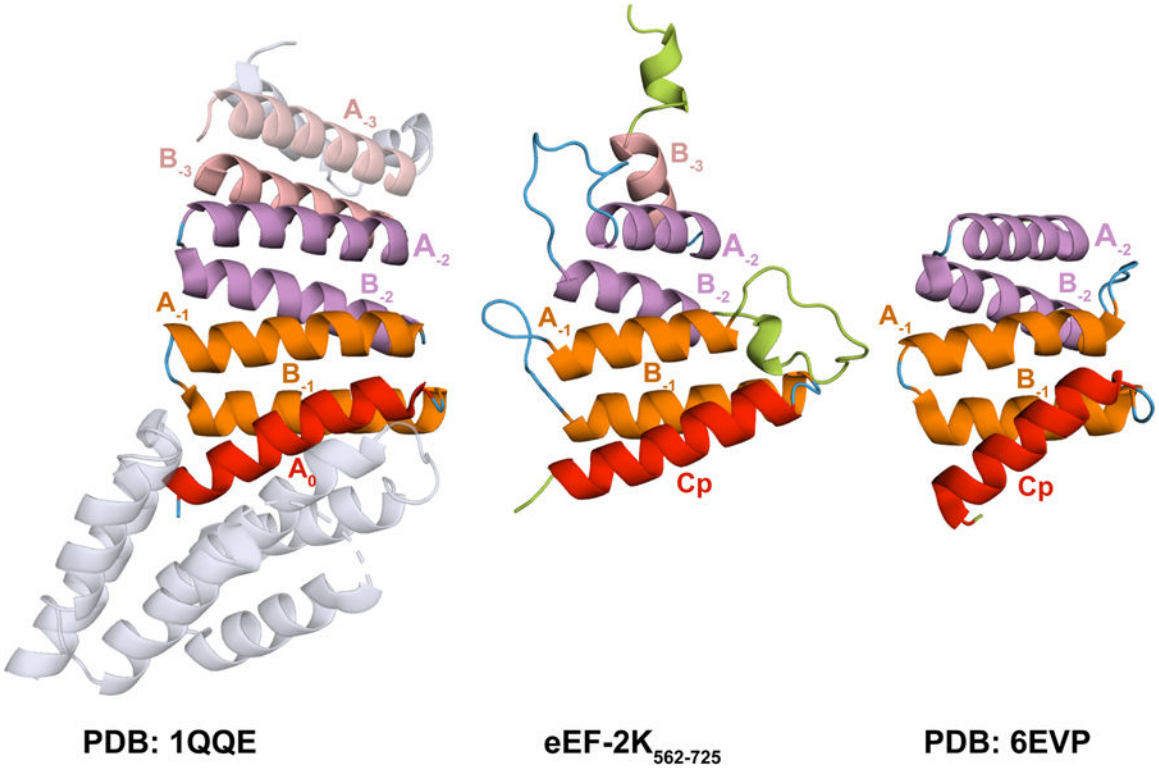

Figure 3.

Representative structural homologs of eEF-2K$_{562–725}$. Comparison of the NMR structure of eEF-2K$_{562–725}$ (middle panel), the crystal structure of Sec17 (left panel) and the crystal structure of human collagen II prolyl 4-hydroxylase (right panel). Corresponding structural regions are colored as in Figure 2. The structures depict the overall arrangement of the helical regions indicative of a tetratricopeptide repeat (TPR) domain. The structure of eEF-2K$_{562–725}$ deviates from a conventional TPR domain given longer loops connecting the helical segments that are similar to those in SEL1-like repeats. The 16-residue $A_{-2}B_{-1}$ loop is significantly longer than those seen in TPR, SEL1-like or similar repeat structures. The orientation of the B_{-3} also diverges from that seen in conventional TPR assemblies.

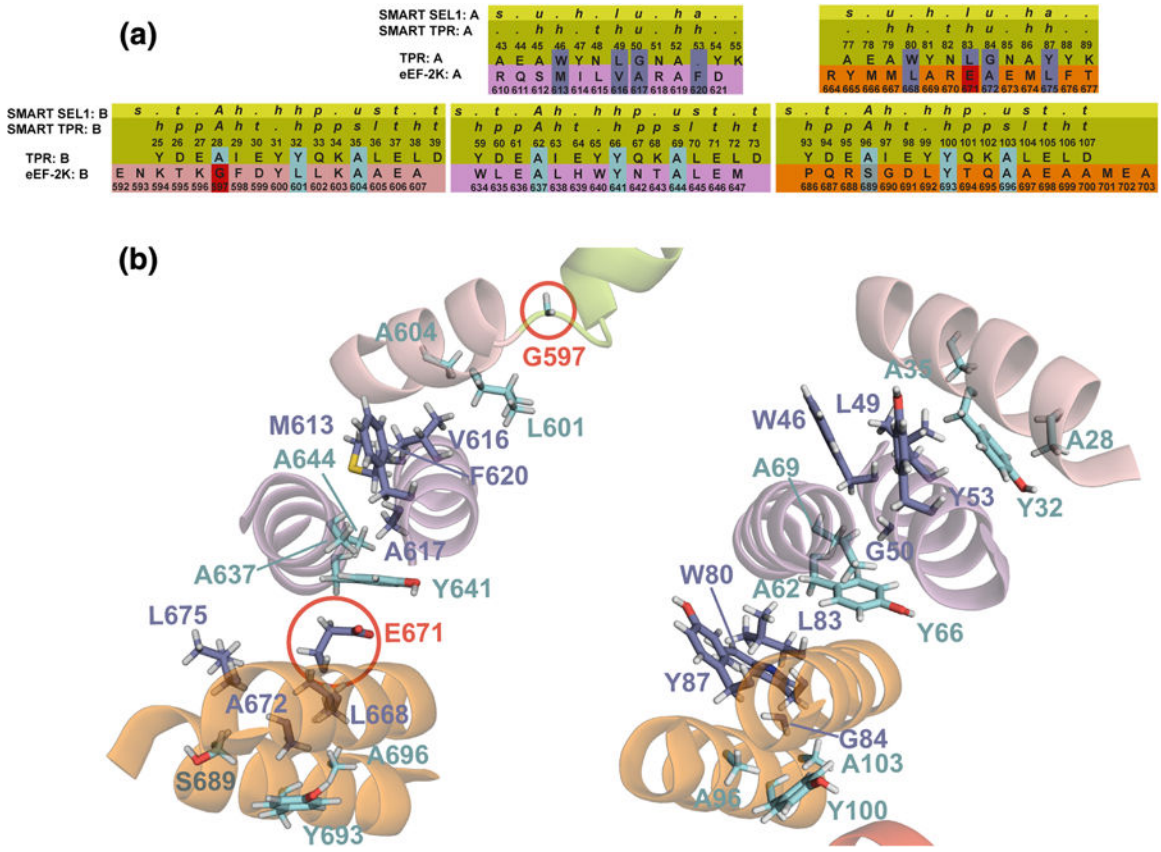

Figure 4.

(A) Alignment of the SMART (80% confidence level) consensus sequences for SEL1-like (yellow) and TPR motifs (dark yellow) are shown along with the sequence of an idealized TPR domain (dark yellow), and the corresponding eEF-2K sequences (based on structure alignment using the DALI server). The sequence for B_{-3} is colored light red, the sequences for A_{-2} and B_{-2} helices are colored magenta, and the sequences for the A_{-1} and B_{-1} helices are colored orange. The positions of the key conserved residues for the A and B helices (as described by Main[38]) are highlighted in blue and cyan, respectively. The divergent, but structurally compatible A96/S689 substitution is shown in dark gray; the divergent A28/G597 and L83/E671 substitutions are highlighted in red. **(B)** The interactions of the core helical modules of eEF-$2K_{562–725}$ (left) and an idealized TPR domain containing two complete repeat units and the B-helix (B_{-3}) of a third repeat are shown. Signature residues are shown in sticks and colored as in **(A)**. The intervening loops are not shown for clarity, and the helices that are colored as above, are partially transparent. The divergent G597 and E671 positions of eEF-$2K_{562–725}$ are circled.

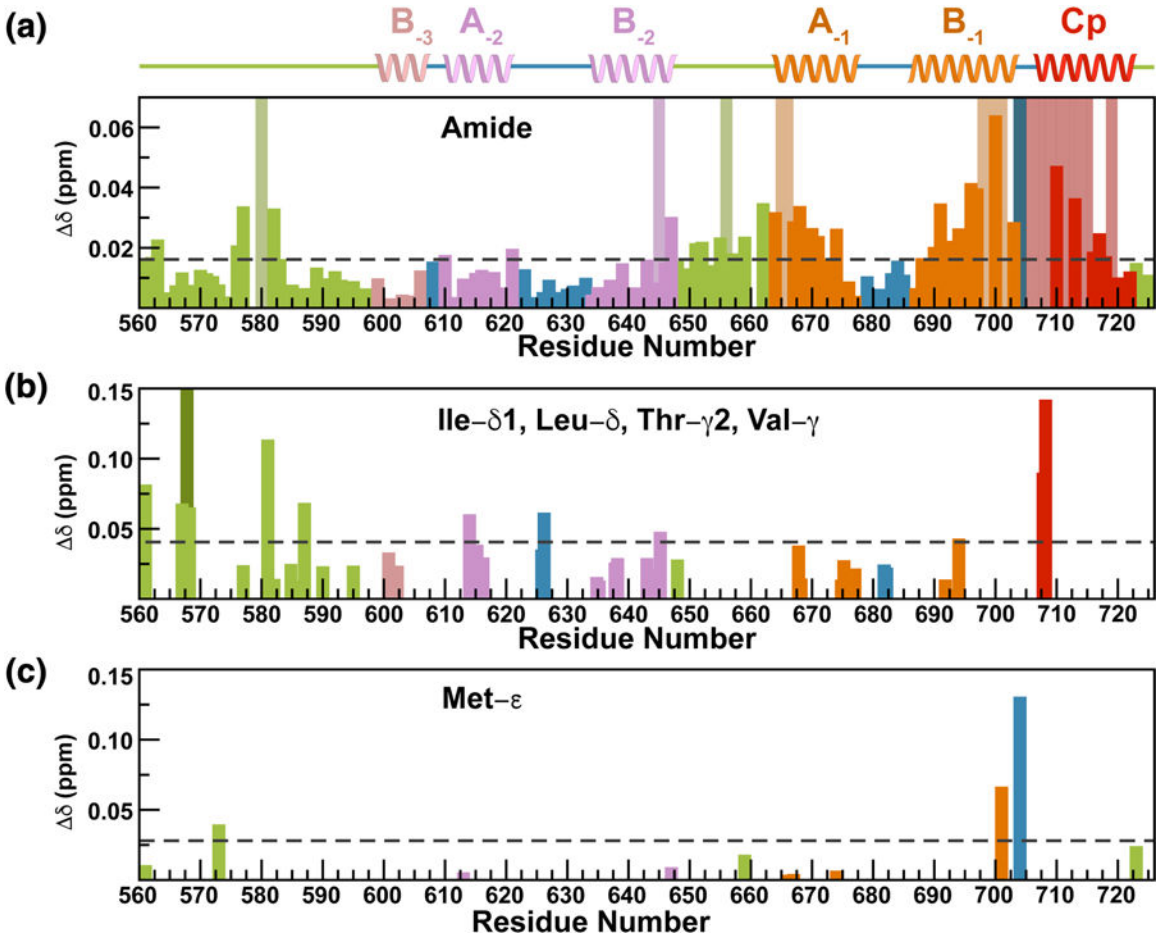

Figure 5.

Chemical shift perturbations (Δδ) detected on eEF-2K$_{562–725}$ in the presence of eEF-2 for backbone amide **(A)**, for Ile–δ_1, Leu–δ, Thr–γ_2 and Val–γ methyl (**B**) and Met–ε methyl (**C**) positions. Leu/Val methyl resonances have not been stereoscopically assigned. The bars represent individual Δδ values and are color coded as defined in Figure 2. Resonances that are broadened to beyond the threshold of detection in the presence of eEF-2 are represented by lighter colored bars of maximum height. The dashed lines indicate threshold values of one standard deviation beyond the mean.

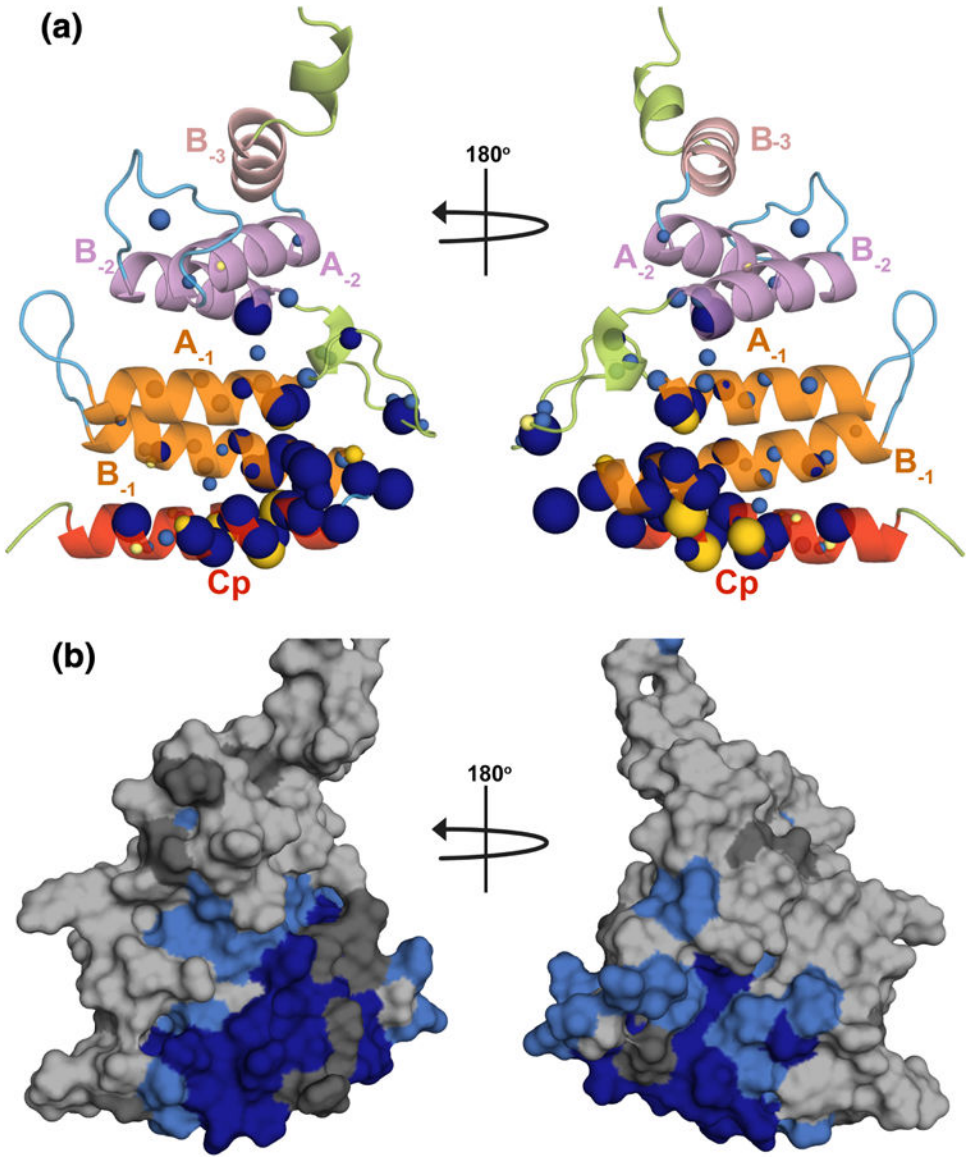

Figure 6.

(A) The distribution of amide and methyl spectral perturbations shown on a ribbon representation of eEF2K$_{562–725}$ colored as in Figure 2. The radii of the spheres are proportional to the magnitude of the perturbations; positions for which the corresponding resonances disappear have the largest radii. Chemical shift perturbations above two standard deviations, including disappearing resonances, are colored dark blue; perturbations within one and two standard deviations are colored in light blue. Yellow spheres (at Cα positions) indicate residues exhibiting significant cross-saturation effects (dark yellow: above two standard deviations; light yellow: between one and two standard deviations; the radius of the sphere is proportional to the magnitude of the cross-saturation effect. **(B)** Surface representation of eEF2K$_{562–725}$ in the same orientation as above. All atoms for a given residue are colored dark blue if at least one moiety within it exhibits either a spectral perturbation or a cross-saturation effect two standard deviations beyond the mean; light blue

if the effect is between one and two standard deviations; and in light grey otherwise. Residues that could not be probed, due to overlapped or missing resonances in the reference state, are colored dark grey. The disordered extreme N-terminus that also shows spectral perturbations in the presence of eEF-2 is omitted from both **(A)** and **(B)** for clarity.

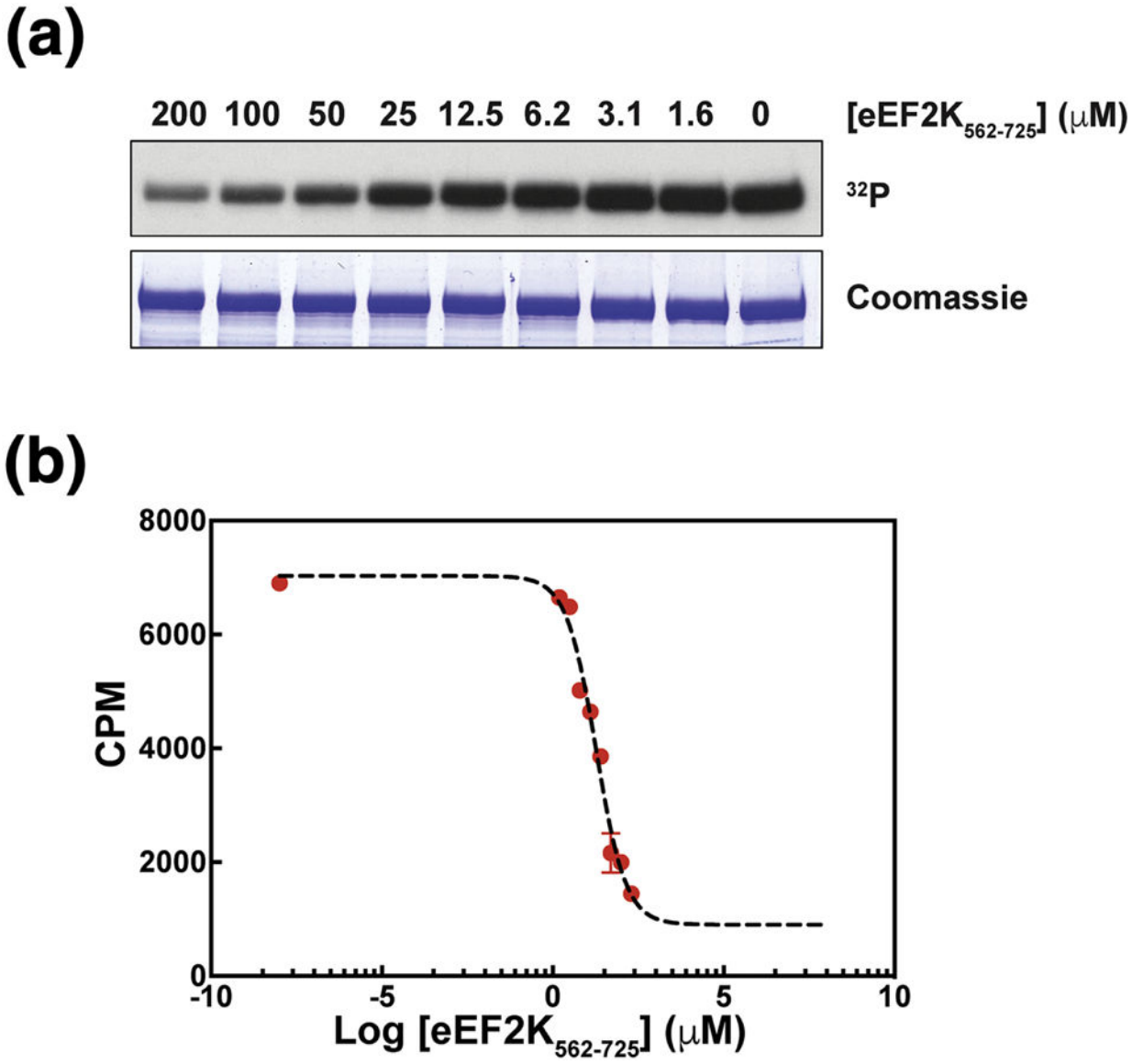

Figure 7.

(A) Phosphorylation of yeast eEF-2 by wild-type full-length eEF-2K in the presence of varying concentrations of eEF-2K$_{562–725}$. SDS-PAGE gels displaying bands corresponding to phosphorylated eEF-2 detected by autoradiography (top) and Coomassie stain (bottom) are shown. **(B)** γ-[^{32}P] incorporation measured by scintillation counting plotted as counts per minute (CPM) as a function of eEF-2K$_{562–725}$ concentration (red circles) and the best fit to Equation 3 (black dashed line).

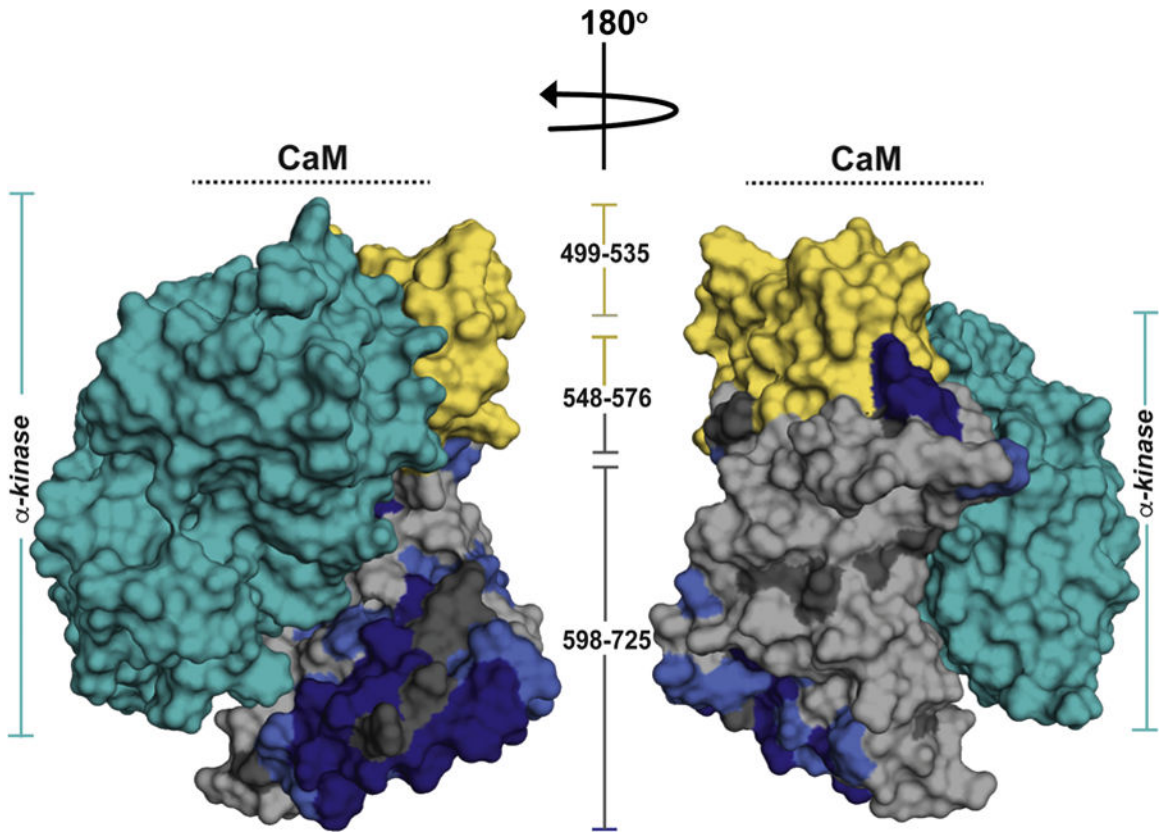

Figure 8.

Surface representation of the orientation of the eEF-2K C-terminal domain (L496-E725) with respect to its α-kinase domain (H103-P330; cyan) using chemical cross-linking mass spectrometry-derived constraints and computational docking[31]. The model incorporates the structure of the eEF-2K$_{562–725}$ (starting from position G597). The modeled region that is not included in the NMR construct (L496-L561) is colored yellow. The G562-E725 region is colored based on the experimentally characterized perturbations induced by eEF-2 binding as described in Figure 6. In this model, the α-kinase domain occludes the core of the concave "cradle" formed by the helical repeats of the CTD. These regions are mostly unperturbed in the presence of eEF-2 in the eEF-2K$_{562–725}$ construct. eEF-2 induced perturbations are in regions that are solvent exposed in the model and distributed on both the concave and convex surfaces of the CTD. Further, some of the perturbed residues within the flexible N-terminus of the eEF-2K$_{562–725}$ construct (L577-L583) are also part of a loop and solvent exposed in the model. This latter region does not appear to contribute a significant amount of binding energy to the eEF-2/eEF-2K$_{562–725}$ interaction. The spatial localization of CaM upon binding eEF-2K is also indicated schematically.

Table 1.

Constraint, Refinement and Structure Statistics for eEF-2K$_{562–725}$

Unambiguous Distance Restraints[1]		
	All	**598–725**
Intra-residue	419	342
Sequential (Δ=|i-j|=1)	313	279
Medium-range (5 > Δ=|i-j| ≥2)	246	242
Long-range (Δ=|i-j| ≥5)	164	164
Dihedral angle restraints (ϕ, ψ)	116	106
RDC, HN (SANI)	70	70
RDC NC' (SANI)	65	65
Cartesian RMSD (Å) from average structure (100 structures)[2]		
	All	**598–725**
Global backbone heavy atoms (N, Cα, C')	6.73 ± 12.6	0.96 ± 1.20
Global sidechain heavy atoms	7.85 ± 12.4	1.91 ± 1.48
Helices; backbone heavy atoms (N, Cα, C')	**0.42 ± 0.13**	
Helices; sidechain heavy atoms	**1.30 ± 0.66**	
Energies, NOE Statistics (100 structures)		
Total (KCal•mol^{-1})	−6509.69±130.68	
Electrostatic (KCal•mol^{-1})	−6112.74± 129.947	
van der Waals (KCal•mol^{-1})	−1245.31± 12.00	
Conformers NOEs RMSD (Å)	0.078 ± 0.003	
PROCHECK Ramachandran statistics (20 lowest-energy structures)[3]		
	All	**598–725**
Most favored regions (%)	83.6	89.3
Additionally allowed regions (%)	14.7	9.8
Generously allowed regions (%)	0.8	0.5
Disallowed regions (%)	0.9	0.4
G-factor, ϕ,ψ	−0.118	−0.06
G-factor, χ1χ1/χ2	−0.14	−0.14
G-factor, all dihedrals	−0.17	−0.11
Average RMS Z-scores (20 lowest energy structures)[3]		
	All	**598–725**
Bond lengths	0.238 ± 0.006	0.225 ± 0.005
Bond angles	0.430 ± 0.008	0.396 ± 0.009
Omega angle restraints (°)	0.608 ± 0.03	0.640 ± 0.03
Side-chain planarity	0.47 ± 0.11	0.47 ± 0.11
Improper dihedral distribution	0.52 ± 0.11	0.51 ± 0.11

Unambiguous Distance Restraints[1]		
	All	**598–725**
Inside/Outside distribution	1.121 ± 0.015	1.059 ± 0.014
1st generation packing quality	−2.35 ± 0.15	−0.91 ± 0.089
2nd generation packing quality	−2.52 ± 0.29	−1.58 ± 0.23
PSVS Z-Scores (20 lowest energy structure structures)[3]		
	All	**598–725**
PROCHECK G-factor ϕ,ψ	0.67	0.94
PROCHECK G-factor, all dihedrals	0.0	0.24
Verify 3D	−3.5±0.015	−1.28±0.02
ProsaII (−ve)	−0.25±0.05	1.12±0.05
MolProbity clashscore	0.34±1.9	0.28±2.4

[1] An additional 430 ambiguous restraints were also present.

[2] Average RMSD per residue with respect to an average structure.

[3] 20 lowest energy structures deposited into the PDB with ID: 6NX4.